Construction of metal/WO$_{2.72}$/rGO ternary nanocomposites with optimized adsorption, photocatalytic and photoelectrochemical properties

Benxia Li*, Xiankun Shao, Tongxuan Liu, Liangzhi Shao, Baoshan Zhang

School of Materials Science and Engineering, Anhui University of Science and Technology, Huainan, Anhui 232001, China

ARTICLE INFO

ABSTRACT

In this work, metal/WO$_{2.72}$/rGO ternary nanocomposites were constructed by a two-step in situ loading process. The binary WO$_{2.72}$/rGO nanocomposite was first prepared by in situ growth of ultrathin WO$_{2.72}$ nanowires on rGO nanosheets via a solvothermal reaction, and the plasmonic metal (Ag and Au) nanoparticles were subsequently loaded on the WO$_{2.72}$/rGO nanocomposite by an in situ redox. For comparison, a series of nanomaterials including the WO$_{2.72}$ nanowires, WO$_{2.72}$/rGO, Ag/WO$_{2.72}$, Au/WO$_{2.72}$, Ag/WO$_{2.72}$/rGO, and Au/WO$_{2.72}$/rGO, were prepared and characterized in detail. These WO$_{2.72}$-containing materials showed very high adsorption capacities to the cationic dye of methylene blue (MB) because of the negatively charged surface of WO$_{2.72}$ nanowires. For the photocatalytic degradation of MB, each of the three components specifically contributes to the performance of the ternary nanocomposite photocatalysts. The WO$_{2.72}$ nanowires provide high adsorption of the target molecules. The metal nanoparticles extend the visible light response range due to their SPR effect and increase the lifetime of the photogenerated electron–hole pairs as well. The rGO nanosheets further increase the adsorption and offer a rapid transferring path for the photogenerated electrons, achieving an efficient charge separation. The ternary nanocomposites showed the highest photocatalytic activity towards degradation of MB and the highest photocurrent when served as photoelectrode materials. The electrochemical impedance spectra (EIS) Nyquist plots also confirmed the highest charge transfer efficiency of the metal/WO$_{2.72}$/rGO ternary nanocomposites. Therefore, the integration of the three components could achieve collective effect to greatly increase the efficiency of visible-light conversion.

© 2016 Elsevier B.V. All rights reserved.

1. Introduction

Solar energy conversion by photocatalysis has been attracting much interest as a promising technology for solving the growing threat from both energy shortage and environmental pollution [1–3]. Semiconductor photocatalytic technique has been widely investigated as one of the most important strategies for fuel production [4], chemical synthesis [5] and environmental remediation [6]. The design of materials with new and improved properties in terms of efficient solar energy conversion is one of the great challenges in materials science and technology. Like in other fields of materials chemistry, developing photocatalysts with optimized performance generally follow the two strategies: (i) the discovery of completely new materials, or (ii) the combination of available materials with additive or synergistic properties [7,8].

Among the available semiconductor photocatalysts, tungsten oxide (WO$_{3-x}$) has presented many merits such as the visible light response because of its narrow band gap of 2.4–2.8 eV, a high resistance to photocorrosion, a deep valence band (+3.1 eV) favoring oxidation reactions, which make it a promising alternative to TiO$_2$ photocatalysts [9–11]. However, like many simple metal oxide semiconductors, a main drawback of WO$_{3-x}$ hinders its application as a practical photocatalyst. The potential of the conduction band of WO$_{3-x}$ (ca. +0.5 V$_{NHE}$ at pH 0) limits the photogenerated electrons to react with electron acceptors and facilitates the recombination of photogenerated electron–hole pairs [12]. Developing more efficient means for electron–hole separation is of crucial importance for achieving higher efficiency conversion of solar energy in photovoltaic and photocatalytic devices. Therefore, one of the important principles to improve the photocatalytic efficiency of

WO_{3-x} is to boost the separation and transfer of the electron–hole pairs [13–15].

Loading noble metal nanoparticles on the semiconductor photocatalysts has been proved as an effectual approach [16–18]. Silver and gold are of special interest for constructing noble metal–semiconductor composite photocatalysts not only because of their electronic effect promoting the separation and migration process of the photogenerated carriers in metal–semiconductor interface [19], but also due to their unique surface plasmon resonance (SPR) effect which can dramatically enhance the visible-light harvesting of photocatalysts [20,21]. Popularly, the Ag and Au nanoparticles have been loaded on some wide band-gap semiconductors such as cerium(IV) oxide (CeO_2) [22,23], titanium(IV) oxide (TiO_2) [24,25], and zinc oxide (ZnO) [26], resulting remarkable visible light response photocatalysis due to surface plasmon resonance (SPR). In these plasmonic metal/semiconductors photocatalysts, the wide band-gap semiconductors only work as an electron transferring material under visible light irradiation because they only responds to UV light. However, if WO_{3-x} is used as a plasmonic metal-supporting material, a broaden visible light response would be achieved because of the two absorption bands from the band-gap excitation of WO_{3-x} (< 450 nm) and SPR of metal nanoparticles (450−650 nm), which is very beneficial to the effective utilization of solar light [12]. However, in binary plasmonic photocatalysts of metal/WO_{3-x}, if electrons are transferred from metal nanoparticles to the conduction band of WO_{3-x} through SPR, the recombination of electron and hole pairs is inescapable. Therefore, the third component with excellent ability for transferring electrons is requisite to further improve the separation of electron-hole pairs. Graphene and its analogs (reduced graphene oxide, rGO) are deemed as ideal supports of photocatalysts because their perfect electrical and redox properties, unique 2-D sp^2 hybrid carbon network structure, and other excellent attributes, such as the large specific surface area and long term stability which can endure the oxidative radical attack during exposure to light [27,28]. Fabrication of graphene-based materials has been known as one of the most feasible strategies to improve the photocatalytic performance [29,30]. As a consequence, an efficient charge separation can be expected by construction of the ternary nanocomposites consisting of plasmonic metal nanoparticles and tungsten oxide nanostructures supported on rGO sheets.

Here we report a preparation of the metal/$WO_{2.72}$/rGO ternary nanocomposites consisting of plasmonic metal (Ag and Au) nanoparticles and ultrathin $WO_{2.72}$ nanowires supported on rGO nanosheets. Each of these three components specifically contributes to the performance of the nanocomposite as a photocatalyst. The tungsten oxide nanowires provide high adsorption of the target molecules, and the metal nanoparticles extend the visible light response range due to their SPR effect and increase the lifetime of the photogenerated electron−hole pairs as well. The rGO nanosheets offer a rapid transferring path for the photogenerated electrons, achieving an efficient charge separation during the photocatalytic process. The metal/$WO_{2.72}$/rGO ternary nanocomposites showed the highest photocatalytic activity towards degradation of MB and the largest photocurrent when served as a photoelectrode material. The electrochemical impedance spectra (EIS) Nyquist plots also confirmed the highest charge transfer efficiency of the metal/$WO_{2.72}$/rGO ternary nanocomposites.

2. Experimental

2.1. Materials

All the chemicals are analytical reagents and are used as received without further purification. Anhydrous tungsten hexachloride (WCl_6), silver nitrate ($AgNO_3$), chloroauric acid tetrahydrate ($HAuCl_4 \cdot 4H_2O$), cetyl-trimethyl ammonium bromide (CTAB), concentrated hydrochloric acid (HCl, 37 wt.%), graphite powder, concentrated sulfuric acid (H_2SO_4, 98 wt.%), hydrogen peroxide aqueous solution (H_2O_2, 30 wt.%), potassium permanganate ($KMnO_4$), and absolute alcohol (C_2H_5OH, EtOH) were commercially obtained from Shanghai Sinopharm Chemical Reagent Co., Ltd. Deionized water was used throughout this work.

2.2. Preparation of $WO_{2.72}$ nanowires and $WO_{2.72}$/rGO nanocomposites

The rGO nanosheets used in our experiments were synthesized by an improved Hummers' method [31]. The as-prepared rGO was dispersed in absolute alcohol by ultrasonic to form a suspension with rGO concentration of 5 mg/mL. The ultrathin $WO_{2.72}$ nanowires with high aspect ratios were prepared by a modified solvothermal method [32]. In our work, 0.03 g of WCl_6 and 0.1 mg of CTAB were dissolved in 40 mL of absolute ethanol by magnetic stirring, forming a homogeneous solution. The solution was transferred into a 50 mL Teflon-lined stainless steel autoclave which was closed and then maintained at 180 °C for 18 h. After that, the autoclave was cooled to room temperature naturally. The formed blue precipitate was collected by centrifugation and washed with absolute alcohol and distilled water to remove the residual surfactants.

For the preparation of $WO_{2.72}$/rGO nanocomposite, 0.378 mL of the rGO suspension (5 mg/mL) was added into the 40 mL solution with 0.03 g of WCl_6 and 0.1 mg of CTAB. The other processing procedures are the same as that for the preparation of $WO_{2.72}$ nanowires. The as-obtained $WO_{2.72}$/rGO nanocomposite has a theoretical content of rGO about 10 wt.%.

2.3. Preparation of metal/$WO_{2.72}$ and metal/$WO_{2.72}$/rGO nanocomposites

The plasmonic metal (Ag and Au) nanoparticles were loaded on the as-prepared $WO_{2.72}$ nanowires and $WO_{2.72}$/rGO nanocomposite, respectively, by an in situ redox [33]. The above-mentioned as-prepared $WO_{2.72}$ nanowires or $WO_{2.72}$/rGO nanocomposite were dispersed in 15 mL of distilled water to form a suspension under magnetic stirring. During the reaction, 56 μL of the metal precursor ($AgNO_3$ or $HAuCl_4$) solution (0.01 M) was added dropwise into the suspension every 4 h in dark and room temperature. After 170 μL of the metal precursor was added, the suspension was stirred unceasingly for 12 h in dark and room temperature. After the reaction, the product was collected by centrifugation and washed with absolute alcohol and deionized water, and then dried in a vacuum oven at 60 °C.

2.4. Characterizations

The field emission scanning electron microscopy (FESEM) images were obtained on a JEOL JSM–6700 F (Japan) at an accelerating voltage of 20 kV. The X-ray diffraction (XRD) patterns were recorded on a Japan Shimadzu XRD-6000 with graphite monochromatized high-intensity Cu Kα radiation (λ = 1.542 Å), and operated at 40 kV voltage and 30 mA current. Transmission electron microscopy (TEM) and high-resolution transmission electron microscopy (HRTEM) images associated with the energy-dispersive X-ray (EDX) spectra were obtained on TEM JEOL-2010 (Japan). X-ray photoelectron spectroscopy (XPS) measurements were performed on a VGESCALAB MKII X-ray photoelectron spectrometer with an exciting source of Mg Kα. Thermal gravimetric analysis (TGA) for every sample was carried out on a SDT-2960 thermal analyzer at a heating rate of 10 °C/min from room temperature to 800 °C in air. The pH values and Zeta potential of

the $WO_{2.72}$ suspension (0.5 wt.% $WO_{2.72}$), which was prepared by dispersing the as-prepared $WO_{2.72}$ nanowires in deionized water, were determined on a Colloidal Dynamics Zeta Probe (USA). The UV–vis absorption spectra of the as-obtained nanomaterials were measured on Shimadzu UV-2600 UV–vis spectrophotometer, by dispersing the powder samples in deionized water. The specific surface areas of the samples were determined by the Brunauer-Emmett-Teller (BET) nitrogen adsorption method using a Micromeritics ASAP 2020 V4.01 (V4.01 E) analyzer (USA).

2.5. The adsorption property and adsorption capacity tests

The adsorption property of the as-prepared photocatalysts was tested by adsorbing cationic organic dye of methylene blue (MB), anionic organic dye of methyl orange (MO), and their mixture from water in dark, respectively. For determining the adsorption capacity (C) of each photocatalyst, 5 mg of the photocatalyst was dispersed into 50 mL of MB aqueous solution (5×10^{-5} mol/L), and take 1 mL of the solution as a sample after stirring for 2 h and 6 h in dark, respectively. The sampled solutions were analyzed by their UV–vis absorption spectra recorded on a Shimadzu UV-2600 spectrophotometer. The specific absorption capacity (C, μmol/g) was calculated by Eq. (1):

$$C = \frac{I_0 - I_6}{I_0} \times \frac{c_0 \times V}{m} \tag{1}$$

where I_0 is the initial absorbance, I_6 is the absorbance after stirring for 6 h, c_0 is the initial concentration (5×10^{-5} mol/L), V is the solution volume (50 mL), and m is the mass of photocatalyst (5 mg). For the selective adsorption test, 25 mL of MB aqueous solution (1×10^{-4} mol/L) and 25 mL of MO aqueous solution (1×10^{-4} mol/L) were mixed, and 5 mg of the photocatalyst was dispersed in the mixed solution. 1 mL of the solution was sampled after stirring for 2 h and 6 h in dark, respectively. The sampled solutions were analyzed by their UV–vis absorption spectra.

2.6. Visible light photocatalytic degradation of organic dyes

The photocatalytic property of the as-prepared materials was evaluated by the photodegradation of organic dyes in water. The photocatalytic degradation was carried out under visible light ($\lambda \geq 420$ nm), which was provided using a 300 W Xe lamp (CEL-HXF300, Beijing China Education Au-light Co., Ltd) equipped with a 420 nm cutoff filter. The light source was positioned approximately 10 cm from the top of the beaker, which was fan-cooled during the experiment. For each test in this work, the illumination intensity was measured to ensure that the light source output was almost unchanged. The optical power density on the reaction solution is measured to be $\sim$72.66 mW/cm^2. In a typical experiment, the photocatalyst (5 mg) was dispersed into 50 mL of MB or MO aqueous solution (5×10^{-5} mol/L) in a Pyrex beaker at room temperature under air. Before the light was turned on, the suspension was continuously stirred for 2 h in dark to achieve an adsorption–desorption equilibrium between the photocatalyst and the dye molecules. The concentration of dye during the degradation process was monitored using a UV–vis spectrophotometer (Shimadzu UV-2600).

2.7. Photoelectrochemical measurements

Photocurrent measurements were performed using a three-electrode configuration, with the as-prepared nanomaterials ($WO_{2.72}$ nanowires, $WO_{2.72}$/rGO, Ag/$WO_{2.72}$, Au/$WO_{2.72}$, Ag/$WO_{2.72}$/rGO, and Au/$WO_{2.72}$/rGO,) as working electrodes, saturated Ag/AgCl as the reference electrode, and a platinum wire as counter electrode. A 1.0 M KOH aqueous solution was used as

the electrolyte. For preparing the working electrode, 5 mg of the photocatalyst was grinded in an agate mortar and then dispersed in 0.5 mL of ethanol. The mixtures were ultrasonically scattered for 30 min to form a suspension. Then, the suspension was spin-coated on an indium tin oxide (ITO) glass (2×4 cm). After the natural drying in air for 12 h, the catalyst film on ITO glass was dried at 120 °C for 5 h, and then used as the working electrode. The ITO glass was firstly ultrasonically cleaned with detergent for 30 min, washed by ultrapure water, and then boiled for 1 h in an aqueous solution of hydrogen peroxide (30 mL), ammonium hydroxide (30 mL) and ultrapure water (180 mL). The ITO glass was soaked into ethanol for use after the final washing with ultrapure water. Before used, the ITO glass was further sterilized with a 254 nm UV light irradiation. An electrochemical workstation (CHI 660D, Shanghai Chenhua, China) was used to measure current–voltage (I–V) characteristics of the electrode. The light irradiation is the same as that used in the photocatalytic degradation of MB. Before photocurrent measurements, the electrolyte was purged with N_2 for 1 h to remove the oxygen in the electrolyte. Impedance measurements were performed in the dark and under the visible light illumination in 0.05 M Na_2SO_4 solution at open circuit voltage.

3. Results and discussion

3.1. Synthesis and characterizations of materials

The procedures for preparations of the various materials including $WO_{2.72}$ nanowires, $WO_{2.72}$/rGO, Ag/$WO_{2.72}$, Au/$WO_{2.72}$, Ag/$WO_{2.72}$/rGO, and Au/$WO_{2.72}$/rGO in the present experiments are illustrated in Scheme 1. The $WO_{2.72}$/rGO binary nanocomposite was prepared by the alcohothermal deposition of $WO_{2.72}$ nanowires on rGO nanosheets. Then, the noble metal precursor ($AgNO_3$ and $HAuCl_4$) solutions were injected into the suspensions of the $WO_{2.72}$ nanowires and the $WO_{2.72}$/rGO nanocomposite, respectively, by a multi-step injection process. The noble metal (Ag and Au) nanoparticles were loaded on the $WO_{2.72}$ nanowires and the $WO_{2.72}$/rGO nanocomposite, respectively, through an in situ redox reaction between weakly reductive $WO_{2.72}$ and oxidative metal salt precursors in aqueous solution [33], to obtain the metal/$WO_{2.72}$ and the metal/$WO_{2.72}$/rGO nanocomposites.

The SEM and TEM images shown in Fig. 1 demonstrate that the as-prepared tungsten oxide nanowires have uniform one-dimensional structures and very high aspect ratio, with diameters of $\sim$10 nm and length up to several micrometers. The nanowires are composed of many individual, thinner nanowires. The dispersion of the tungsten oxide nanowires in water shows a blue color (inset in Fig. 1a). The XRD pattern (Fig. S1, Supporting Information) confirms the tungsten oxide nanowires belong to the monoclinic structure type $WO_{2.72}$ (JCPDS no. 65-1291). SEM and TEM images in Fig. 2a and b reveal the morphology of the as-obtained $WO_{2.72}$/rGO binary nanocomposite. A layer of tungsten oxide nanowires are attached
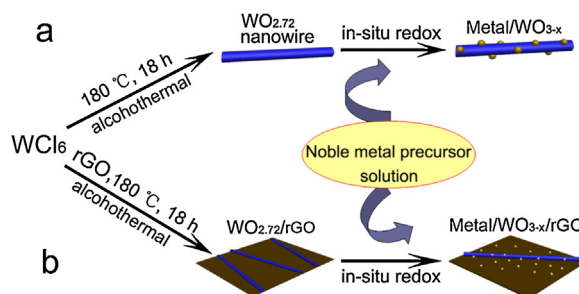
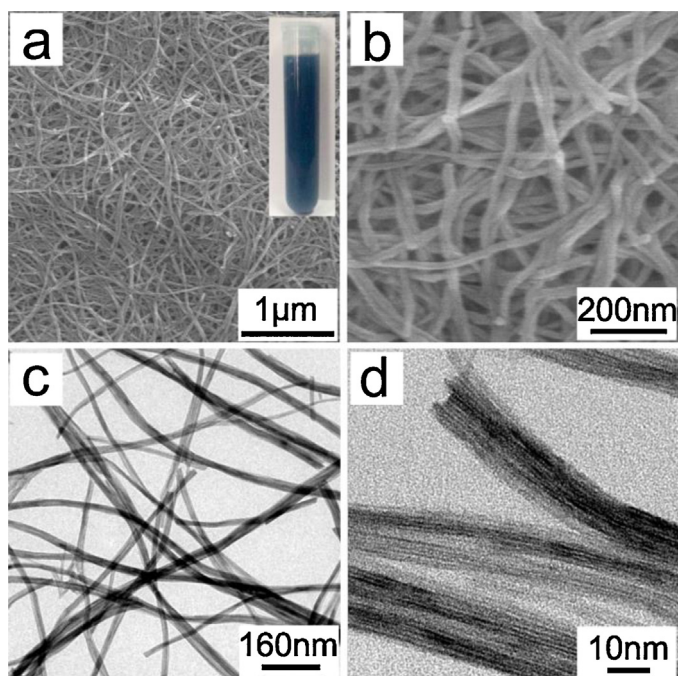**Scheme 1.** Illustration of the procedures for preparations of the materials in our experiments.

Fig. 1. (a, b) SEM images, and (c, d) TEM images of the $WO_{2.72}$ nanowires with different magnifications. Inset is a photograph of the $WO_{2.72}$ nanowires dispersed in water.
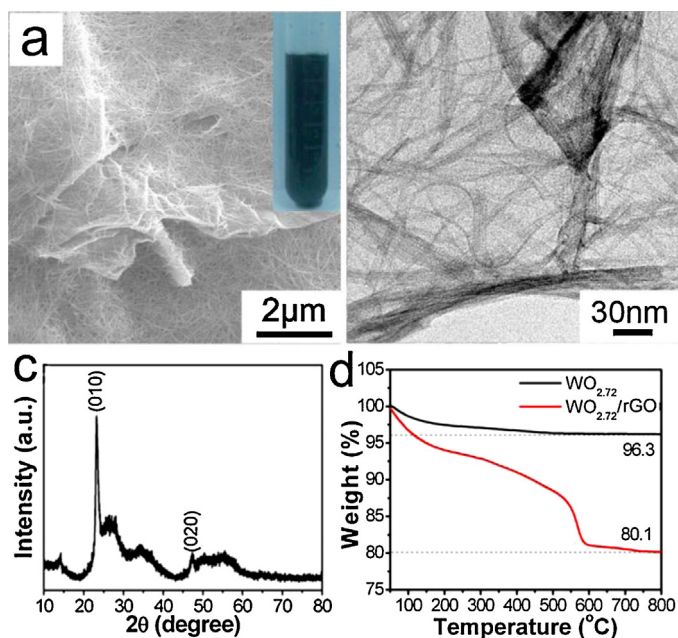

Fig. 2. (a) SEM image, (b) TEM image, and (c) XRD pattern of the $WO_{2.72}$/rGO binary nanocomposite. (d) TGA curves of pure $WO_{2.72}$ nanowires and the $WO_{2.72}$/rGO nanocomposite. Inset is a photograph of the $WO_{2.72}$/rGO nanocomposite dispersed in water.

on rGO nanosheets. The nanowires layer remains tightly on the rGO nanosheets after the ultrasonic treatment for SEM and TEM sample preparations, suggesting the strong combination between nanowires and rGO nanosheets. The dispersion of the $WO_{2.72}$/rGO nanocomposite in water presents a black color (inset in Fig. 2a) because of the incorporation of rGO. XRD pattern (Fig. 2c) of the nanocomposite presents mainly two intense diffraction peaks, corresponding to the (010) and (020) crystal faces of the monoclinic $WO_{2.72}$ (JCPDS no. 65-1291). Thermogravimetric analysis was used

to determine the content of rGO in the binary nanocomposite. The TGA curves of pure $WO_{2.72}$ nanowires and the $WO_{2.72}$/rGO nanocomposite are shown in Fig. 2d. The total weight loss of the pure $WO_{2.72}$ nanowires is about 3.7% up to 500 °C in air, due to the removal of absorbed water and some surface hydroxyls. The total weight loss of the $WO_{2.72}$/rGO nanocomposite is about 19.9% up to 700 °C in air, which is attributed to the combustion of rGO component as well as the removal of absorbed water. The rGO content percent (M) in the nanocomposite was calculated to be 16.2 wt.% according to the residual weight percent of the composite (W) and pure $WO_{2.72}$ nanowires (n), by using the following Eq. (2) [34]

$$(2) \quad (1 - M) \times n = W$$

Subsequently, the plasmonic metal (Ag and Au) nanoparticles were loaded on both the $WO_{2.72}$ nanowires and the $WO_{2.72}$/rGO nanocomposite, respectively, through the in situ redox reaction between $WO_{2.72}$ and metal salt precursors in aqueous solution at room temperature. The metal/$WO_{2.72}$ binary nanocomposites (Fig. 3) and the metal/$WO_{2.72}$/rGO ternary nanocomposites (Fig. 4) were obtained respectively. In the SEM images of the metal/$WO_{2.72}$ binary nanocomposites shown in Fig. 3a and d, some bright white particles with sizes of 10–30 nm are attached on the nanowires. The TEM images (Fig. 3b and e) further confirm the loading of metal nanoparticles on tungsten oxide nanowires. The XRD patterns shown in Fig. 3c and f are the same as that of the $WO_{2.72}$ nanowires except the presence of the (111) crystal faces of the cubic phase of metallic Ag (JCPDS No. 89-3722) and metallic Au (JCPDS No. 89-3697), respectively, which confirm these as-obtained binary nanocomposites are Ag/$WO_{2.72}$ and Au/$WO_{2.72}$. Due to the loading of metal nanoparticles, the Ag/$WO_{2.72}$ and Au/$WO_{2.72}$ nanocomposites dispersed in water present brown (the inset in Fig. 3c) and light magenta (the inset in Fig. 3f), respectively.

Fig. 4 demonstrates the microstructures and components of the metal/$WO_{2.72}$/rGO ternary nanocomposites. The morphologies of the ternary nanocomposites are similar to those of the $WO_{2.72}$/rGO binary nanocomposites. Lots of $WO_{2.72}$ nanowires are attached on rGO nanosheets and interlaced with each other. Besides, numerous nanoparticles are clearly observed on both $WO_{2.72}$ nanowires and rGO nanosheets, and they should be the loaded metal nanoparticles. The metal nanoparticles have small sizes and a very narrow size distribution. Moreover, the Ag nanoparticles in Fig. 4a and b present a smaller size of ∼30 nm than that of Au nanoparticles (∼50 nm) in Fig. 4d and e. XRD patterns (Fig. 4c and f) show the presences of the monoclinic $WO_{2.72}$ as well as the cubic Ag or Au metal. The diffraction intensity of Au particles in Au/$WO_{2.72}$/rGO nanocomposite is stronger, may because of the larger size of Au nanoparticles. Both of Ag/$WO_{2.72}$/rGO and Au/$WO_{2.72}$/rGO samples dispersed in water present black color due to the existence of rGO. More detailed information was typically obtained from HRTEM images and energy-dispersive X-ray spectra (EDX) of the Au/$WO_{2.72}$/rGO ternary nanocomposite, as shown in Fig. 5. The low-magnification TEM image in Fig. 5a shows the metal-nanoparticles-loading nanowires supported on rGO nanosheets. The HRTEM image (Fig. 5b) recorded on a nanowire in Fig. 5a exhibits well-resolved lattice fringe with the spacing of 0.376 nm, corresponding to the interplanar spacing of (010) lattice plane of the monoclinic $WO_{2.72}$. The other HRTEM image (Fig. 5c) recorded on a nanoparticle in Fig. 5a exhibits well-resolved lattice fringe with the spacing of 0.235 nm, corresponding to the interplanar spacing of (111) lattice plane of the cubic Au metal. Moreover, the HRTEM image shown in Fig. 5d demonstrates the Au nanoparticle loading on $WO_{2.72}$ nanowire. The EDX spectra recorded on the nanowire area (Fig. 5e) and the nanoparticle area (Fig. 5f) further confirm their corresponding components of tungsten oxide and Au, respectively. The elemental compositions and chemical states of
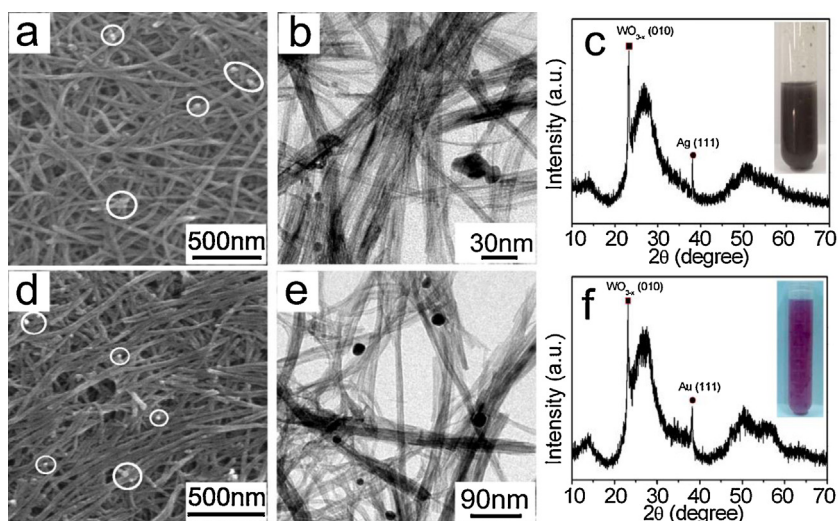
Fig. 3. (a–c) Ag/WO$_{2.72}$ binary nanocomposites: (a) SEM image, (b) TEM image, (c) XRD pattern, and the inset of c is a photograph of this sample dispersed in water. (d-f) Au/WO$_{2.72}$ binary nanocomposite: (d) SEM image, (e) TEM image, (f) XRD pattern, and the inset of *f* is a photograph of this sample dispersed in water.
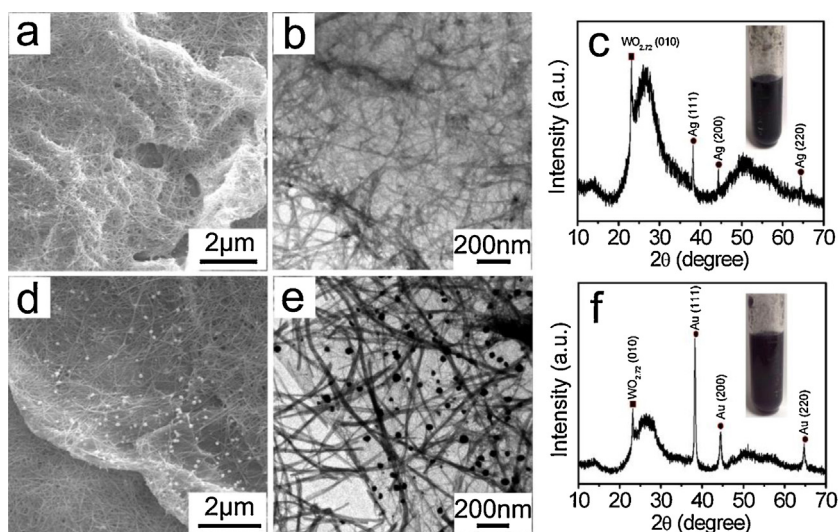

Fig. 4. (a–c) Ag/WO$_{2.72}$/rGO ternary nanocomposites: (a) SEM image, (b) TEM image, (c) XRD pattern, and the inset of *c* is a photograph of this sample dispersed in water. (d–f) Au/WO$_{2.72}$/rGO ternary nanocomposite: (d) SEM image, (e) TEM image, (f) XRD pattern, and the inset of *f* is a photograph of this sample dispersed in water.
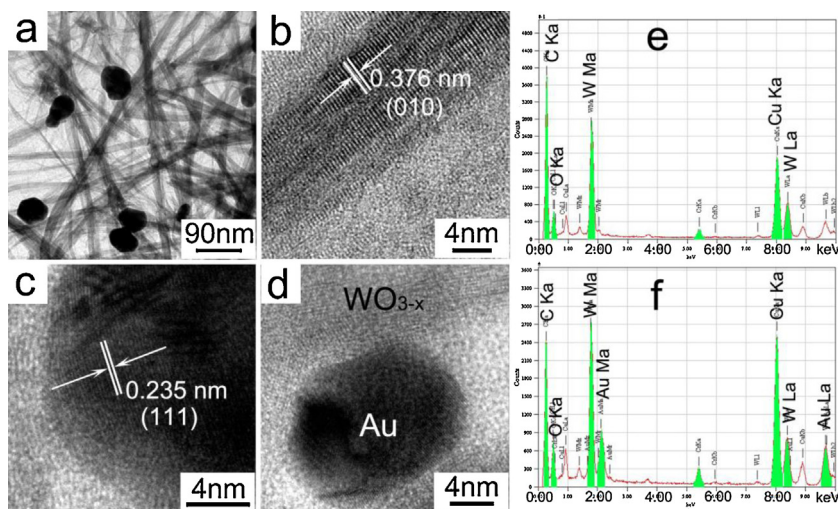

Fig. 5. Au/WO$_{2.72}$/rGO ternary nanocomposite. (a) A low-magnification TEM image, (b) HRTEM image of a WO$_{2.72}$ nanowire, (c) HRTEM image of Au nanoparticle, (d) HRTEM image of the interface between Au nanoparticle and WO$_{2.72}$ nanowire, (e) EDX spectrum recorded on the nanowire area, (f) EDX spectrum recorded on the nanoparticle area.
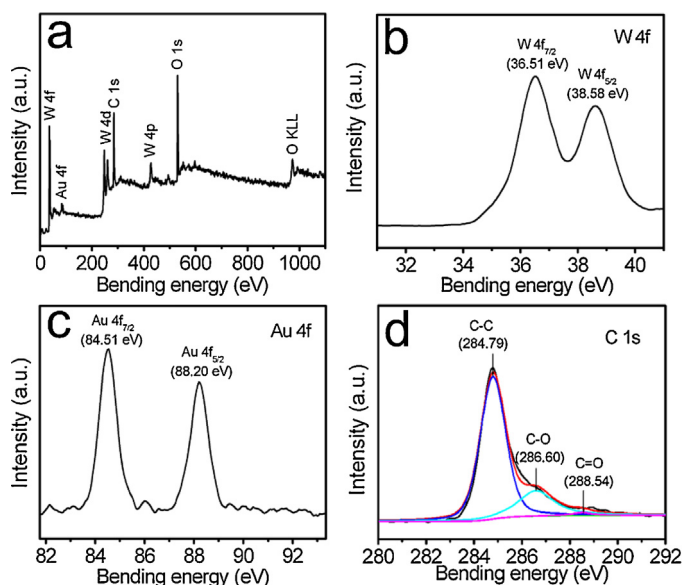
Fig. 6. XPS spectra of the Au/WO$_{2.72}$/rGO ternary nanocomposite. (a) Survey spectrum, (b) W 4f peaks, (c) Au 4f peaks, and (d) C 1s peak.
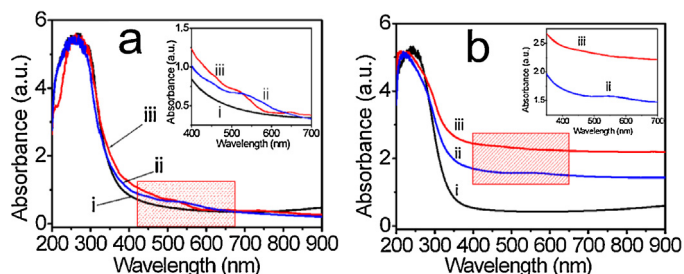

Fig. 7. UV–vis absorption spectra of the different samples dispersed in water. (a-i) WO$_{2.72}$ nanowires, (a-ii) Au/WO$_{2.72}$ nanocomposite, (a-iii) Ag/WO$_{2.72}$ nanocomposite; (b-i) WO$_{2.72}$/rGO nanocomposite, (b-ii) Au/WO$_{2.72}$/rGO nanocomposite, (b-iii) Ag/WO$_{2.72}$/rGO nanocomposite. The inserts are the enlarged observation of the framework-marked area, respectively.

the Au/WO$_{2.72}$/rGO ternary nanocomposite were typically investigated by XPS characterization. The XPS survey spectrum (Fig. 6a) shows the presence of W, O, Au and C elements. No other impurity element exists. The high resolution spectrum (Fig. 6b) of W 4f with specific peaks at 36.51 eV and 38.58 eV for 4f$_{7/2}$ and 4f$_{5/2}$, respectively, indicates the dominating oxidation state of surface atomic W is W^{6+} [32]. Fig. 6c shows the high resolution Au 4f spectrum of the Au nanoparticles in the nanocomposite, presenting two individual peaks at 84.51 eV for Au 4f$_{7/2}$ and at 88.20 eV for Au 4f$_{5/2}$, which confirms the formation of metallic Au^0 [35]. The C1s spectrum (Fig. 6d) of rGO in this nanocomposite indicates that the carbon atoms have three combination states, the dominating non-oxygenated C—C bond (284.79 eV), a small quantity of the epoxy and hydroxyl (C—O, 286.6 eV) and the carbonyl C=O (288.54 eV) [36].

Fig. 7 shows the UV–vis absorption spectra of the different samples dispersed in water, including WO$_{2.72}$ nanowires, Au/WO$_{2.72}$, Ag/WO$_{2.72}$, WO$_{2.72}$/rGO, Au/WO$_{2.72}$/rGO, and Ag/WO$_{2.72}$/rGO. The inserts are the enlarged observation of the framework-marked areas. By comparison, the pure WO$_{2.72}$ nanowires and the WO$_{2.72}$/rGO nanocomposite present similar light absorption feature. They have a strong absorption in 200–380 nm wavelength due to the inter-band absorbance and a weak absorption in near-infrared region (>800 nm) due to the charge transfer between the defect states (W^{+5} → W^{+6}, O → W^{+5}/W^{+6}) [37]. While both the
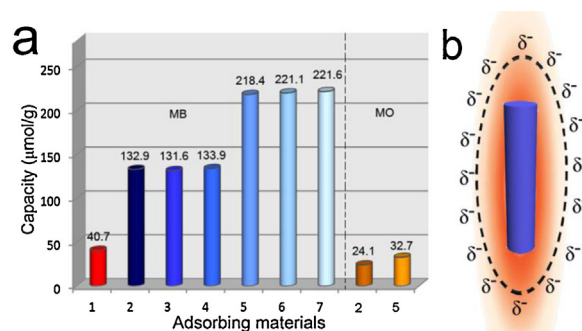

Fig. 8. (a) Specific adsorption capacities of various photocatalysts: 1. α-MoO$_3$ nanowires in Ref. [52], 2. WO$_{2.72}$ nanowires, 3. Ag/WO$_{2.72}$, 4. Au/WO$_{2.72}$, 5. WO$_{2.72}$/rGO, 6. Ag/WO$_{2.72}$/rGO, 7. Au/WO$_{2.72}$/rGO. (b) Schematic presentation of the negative surface charges of WO$_{2.72}$ nanowires.

metal/WO$_{2.72}$ and metal/WO$_{2.72}$/rGO nanocomposites also present a weak absorption in the range of 450–600 nm, which result from the localized surface plasmon resonance (LSPR) of Au or Ag nanoparticles loaded in the nanocomposites. The LSPR peaks of the metal nanoparticles in these nanocomposites broaden obviously because the metal nanoparticles have a wide particle size distribution [38]. Besides, the band gaps of these WO$_{2.72}$-containing nanomaterials were attempted to determine by their UV–vis diffuse reflection spectra. The results obtained from the plots of $(\alpha h\nu)^2$ versus photon energy ($h\nu$) are shown in Fig. S2 (Supporting Information). The band gaps (2.83 ± 1 eV) of the nanocomposites mainly correspond to that of the WO$_{2.72}$ component. The incorporation of metal nanoparticles and rGO in the nanocomposites could extend the visible light absorption range but not change much the band gap of the WO$_{2.72}$ component.

3.2. Selective adsorption and photocatalytic degradation of organic dyes

For practical large-scale applications of semiconductor photocatalysis in hazardous pollutant removal under natural sunlight, the high adsorption capability of the photocatalyst is important because it can enable the photocatalyst to behave as a collector to gather the pollutants when the sun is not shining [39]. Moreover, the preliminary adsorption of pollutant molecules is prerequisite for efficient surface photocatalytic degradation reactions. To verify the adsorption capacity of our as-prepared various WO$_{2.72}$-containing nanomaterials, we tested the adsorption to the typical cationic organic dye of methylene blue (MB), anionic organic dye of methyl orange (MO), and their mixture over the various materials, respectively. The model pollutants were all dissolved in water to form an aqueous solution with an initial concentration of 5×10^{-5} mol/L. The α-MoO$_3$ nanowires with a high adsorption to organic dye reported previously [40] was used as reference for comparison. When only 5 mg of the photocatalyst was dispersed into 50 mL of MB aqueous solution in dark, an obvious decrease in the MB concentration was observed (Fig. S3, Supporting Information). From 2 h to 6 h, the MB concentration decreased very slowly. The adsorption of the photocatalyst at 6 h can be assumed to be saturated. Therefore, the specific adsorption capacity of each photocatalyst was calculated, as shown in Fig. 8a. The WO$_{2.72}$ nanowires and metal/WO$_{2.72}$ nanocomposites have approximate adsorption capacities about 132 μmol/g. Incorporation of rGO could further increase the adsorption capacity of the materials. The WO$_{2.72}$/rGO and metal/WO$_{2.72}$/rGO nanocomposites possess approximate adsorption capacities about 220 μmol/g for adsorbing MB. The results indicate that these WO$_{2.72}$-containing materials present very high adsorption capacity to the cationic dye of MB,

much larger than that of the α-MoO_3 nanowires reported in our previous work. Moreover, the specific surface areas of pure $WO_{2.72}$ nanowires, $Ag/WO_{2.72}$, $Au/WO_{2.72}$, $WO_{2.72}/rGO$, $Ag/WO_{2.72}/rGO$, and $Au/WO_{2.72}/rGO$ nanocomposites are determined to be 65.66, 62.26, 61.32, 105.66, 103.15, and 101.69 m^2/g, respectively. The adsorption capacity of the $WO_{2.72}$-containing materials is almost proportional to their specific surface areas. However, these $WO_{2.72}$-containing materials present very little adsorption towards the anionic dye of methylene orange (Fig. S4, Supporting Information). Such a selective adsorption property can be used to separate the molecules or ions with different charges from aqueous solution. When 5 mg of the photocatalyst was dispersed into 50 mL of MB and MO mixed aqueous solution, in which the initial concentrations of both MB and MO are 5×10^{-5} mol/L, the characteristic absorption intensity of MB at 660 nm dropped dramatically, but that of MO at 465 nm increased a little instead (Fig. S5, Supporting Information). Moreover, the color of the solution changed from blue to greenish orange, suggesting the selective adsorption to the cationic dye. The high adsorption capacity of the $WO_{2.72}$-containing nanomaterials towards the cationic dye of MB is a result of the highly negative surface charges of $WO_{2.72}$ nanowires, as shown in Fig. 8b. The Zeta potential was tested in a $WO_{2.72}$ nanowires suspension (0.5 wt.%, pH = 4.69) to be -2.82 eV, showing that the $WO_{2.72}$ nanowires present negative surface charge even in acidic solution. The negative charges of $WO_{2.72}$ nanowires are from the abundant oxygen-containing groups on the surface, such as W=O and $-O-$, which played a key role in the removal of cationic dye. The integration of high adsorption capacity towards cationic dye and the photocatalytic nature of tungsten oxide will endow the $WO_{2.72}$-containing nanomaterials a strong candidate for subsequent photodegradation of adsorbed MB in water.

To examine the photocatalytic performance of these $WO_{2.72}$-containing nanomaterials for degrading organic dyes, the photocatalytic degradation of MB was carried out firstly. The photocatalytic reactions were carried out under a visible light ($\lambda \geq 420$ nm) from a Xe lamp equipped with a 420 nm cutoff filter. Fig. S6 (Supporting Information) shows the time-dependent absorption spectra of MB solution in the presence of different photocatalysts, where the time "-120 min" means the dark treatment to reach the adsorption–desorption equilibrium between the photocatalyst and MB molecules. The results of the MB degradation in a series of experimental conditions are summarized in Fig. 9a, where C_0 and C_t are the initial concentration after the equilibrium adsorption and the residual concentration of MB, respectively. The degradation of MB in the presence of $WO_{2.72}$ nanowires is 86.1% after 120 min of irradiation. The $WO_{2.72}$ nanowires loaded with metal nanoparticles exhibit higher photocatalytic efficiencies. Moreover, the photocatalytic efficiency could be further improved by introducing rGO nanosheets in the nanocomposites. 99.9% of MB was photodegraded over the metal/$WO_{2.72}$/rGO tannery nanocomposites after 120 min of visible-light irradiation. The initial pH value of the MB solution before exposing irradiation is 5.39, approximate to that of the deionized water (5.60) used in our experiments. After the degradation, the pH value of the solution declined to 4.17, presenting weak acidic due to the acidic degradation products. Fig. 9b shows the kinetic linear fitting curves of photocatalytic degradation of MB under different conditions. It is clear that the curves with irradiation time as abscissa and $\ln(C_t/C_0)$ as the vertical ordinate are linear. The reaction rate constant (k) values corresponding to various $WO_{2.72}$-containing photocatalysts are listed in Table 1. As a result, the ternary nanocomposites of metal/$WO_{2.72}$/rGO showed the highest photocatalytic activity towards degradation of MB. In addition, the photocatalytic activity of the present photocatalysts towards degradation of MO was also tested. The results (Fig. S7, Supporting Information) indicate that all of the photocatalysts are photocatalytically inactive for degradation of MO, validating
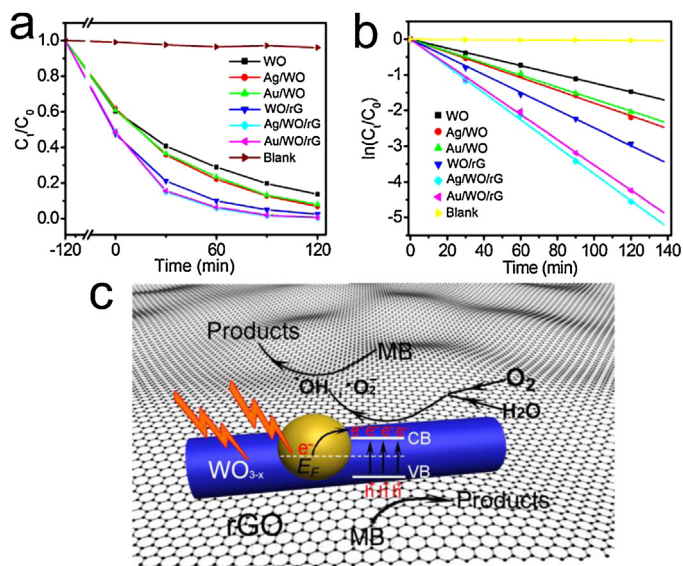

Fig. 9. (a) The concentration changes and (b) the kinetic linear simulation curves of photocatalytic degrading MB in water under visible light over different photocatalysts, where WO is abbreviation of $WO_{2.72}$ nanowires, and rG is abbreviation of rGO, respectively. (c) Schematic mechanism of the photocatalytic degradation of MB over the metal/$WO_{2.72}$/rGO ternary nanocomposite under visible light.

that the adsorption of dye molecules on photocatalyst is a prerequisite for photodegradation. That is, the selective adsorption property of these $WO_{2.72}$-containing photocatalysts results in their selective photocatalysis for degrading organic dyes. In the photocatalytic degradation of MB, the enhanced photocatalysis of the ternary nanocomposites can be attributed to the synergistic effect of the three components. Each of these three components specifically contributes to the performance of the nanocomposite. Firstly, both the $WO_{2.72}$ nanowires and the rGO nanosheets provide high adsorption to MB molecules. Then, the photogenerated carriers were formed through the excitations of both the band-gap transition of $WO_{2.72}$ nanowires and the SPR of metal nanoparticles upon the visible light irradiation. The metal nanoparticles enhanced the visible light harvesting due to their SPR properties. The rGO nanosheets offered a rapid transferring path for the photogenerated electrons, achieving an efficient charge separation during the photocatalytic process. The injected electrons in rGO sheets can be subsequently captured by the absorbed O_2 and H_2O to produce the reactive oxygen species such as $^\bullet O_2^-$ and $^\bullet OH$ [41]. Besides, valence band holes (h^+) of $WO_{2.72}$ can work for the oxidation of the adsorbed MB molecules. Alternatively, h^+ can also oxidize surface H_2O to form reactive $^\bullet OH$, which subsequently oxidize adsorbed organics [13,42]. Therefore, the reactive oxidation species including $^\bullet O_2^-$, $^\bullet OH$, and h^+ participated in degrading MB molecules. Based on the above discussions, a possible mechanism for the photocatalytic degradation of MB over the metal/$WO_{2.72}$/rGO ternary nanocomposite under visible light irradiation was illustrated in Fig. 9c.

3.3. Photoelectrochemical measurements

Photoelectrochemical performances of different $WO_{2.72}$-containing nanomaterials have been compared using chronoamperometric technique in a fixed +0.5 V potential under the intermittent visible light. Fig. 10a and 10b show the photocurrent of the various $WO_{2.72}$-containing samples tested under on–off cycle illumination conditions. The photocurrent of pure $WO_{2.72}$ nanowires (0.005 A/m^2) is very low, hinting the low photon-to-current conversion efficiency of this sample. The photocurrent was improved to different degrees by introducing

Table 1
The reaction rate constant (k) values of the MB photodegradation over various $WO_{2.72}$-containing photocatalysts.

Photocatalyst	$WO_{2.72}$	$Ag/WO_{2.72}$	$Au/WO_{2.72}$	$WO_{2.72}/rGO$	$Ag/WO_{2.72}/rGO$	$Au/WO_{2.72}/rGO$
k (min^{-1})	0.012	0.018	0.017	0.025	0.038	0.035
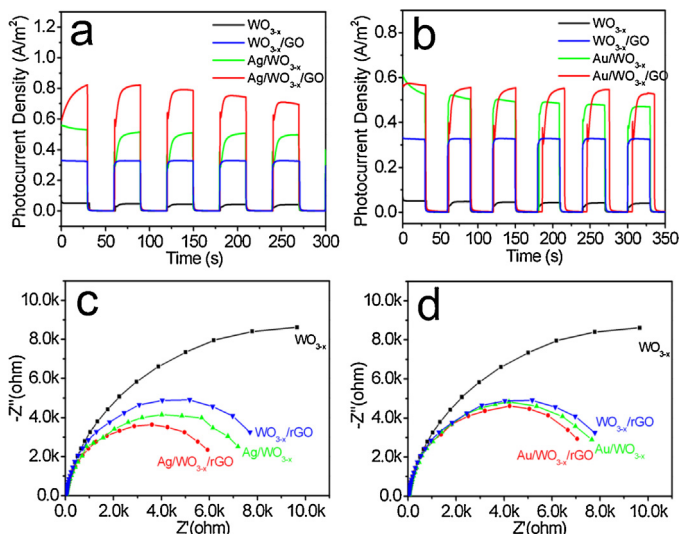
Fig. 10. (a, b) I–t curves of the different samples at an applied potential of 0.5 V vs. Ag/AgCl under the illumination of visible light with wavelength $\lambda \geq 420$ nm with on/off cycles; (c, d) Nyquist plots of electrochemical impedance spectra of the different samples irradiated by a visible light.

rGO nanosheets or plasmonic metal (Ag and Au) nanoparticles. Upon illumination, the $WO_{2.72}/rGO$, $Ag/WO_{2.72}$ and $Au/WO_{2.72}$ binary nanocomposites present higher photocurrents of 0.033, 0.054, and 0.053 A/m^2, respectively. Furthermore, the ternary nanocomposites of metal/$WO_{2.72}$/rGO, $Ag/WO_{2.72}$/rGO in particular, show the highest photocurrent of 0.082 A/m^2 under the visible light illumination. The photocurrents of these nanomaterials under illumination increases with the following sequence order: $WO_{2.72}$ nanowires < $WO_{2.72}/rGO$ < $Ag/WO_{2.72}$ ≈ $Au/WO_{2.72}$ < $Au/WO_{2.72}/rGO$ < $Ag/WO_{2.72}/rGO$. The results are almost in agreement with their photocatalytic performance, confirming that the metal/$WO_{2.72}$/rGO ternary nanocomposites possess highest visible light conversion efficiency. The interfacial properties between the photoelectrode and the electrolyte have been further probed. Fig. 10c and d display the Nyquist plot of electrochemical impedance spectroscopy (EIS). In the Nyquist plot, a semicircle at high frequency represents the charge-transfer process, and the diameter of the semicircle reflects the charge-transfer resistance [43]. Obviously, the semicircle diameters of the present nanomaterials under the visible light illumination follow the sequence order: $WO_{2.72}$ nanowires > $WO_{2.72}/rGO$ > $Ag/WO_{2.72}$ ≈ $Au/WO_{2.72}$ > $Au/WO_{2.72}/rGO$ > $Ag/WO_{2.72}/rGO$. The diameters of the semicircles for the metal/$WO_{2.72}$/rGO ternary nanocomposites, $Ag/WO_{2.72}$/rGO in particular, are much smaller than those of the other samples, indicating the ternary nanocomposites have highest electron mobility. By comparison, the photoelectrochemical performances further confirm the synergistic effect of the three components in metal/$WO_{2.72}$/rGO which specifically contributes to the photocatalytic performance.

4. Conclusions

In summary, we have synthesized the metal/$WO_{2.72}$/rGO ternary nanocomposites by in situ loading the plasmonic metal (Ag

and Au) nanoparticles on the $WO_{2.72}$/rGO nanocomposite which was first prepared by growth of ultrathin $WO_{2.72}$ nanowires on rGO via a solvothermal reaction. For comparison, a series of nanomaterials including $WO_{2.72}$ nanowires, $WO_{2.72}/rGO$, $Ag/WO_{2.72}$, $Au/WO_{2.72}$, $Ag/WO_{2.72}/rGO$, and $Au/WO_{2.72}/rGO$, were prepared and characterized. The $WO_{2.72}$-containing materials showed selective adsorption and photocatalysis for removal of the cationic dye because of the negatively charged surface of $WO_{2.72}$ nanowires. Moreover, the ternary nanocomposites of metal/$WO_{2.72}$/rGO showed the highest photocatalytic activity towards degradation of MB and the highest photocurrent when served as photoelectrode materials. The electrochemical impedance spectra (EIS) Nyquist plots also revealed the highest electron mobility of the metal/$WO_{2.72}$/rGO ternary nanocomposites. In metal/$WO_{2.72}$/rGO nanocomposites, each of the three components specifically contributes to the performance of the ternary nanocomposites as a photocatalyst. The $WO_{2.72}$ nanowires provide high adsorption of the target molecules, and the metal nanoparticles extend the visible light response range due to their SPR effect and increase the lifetime of the photogenerated electron−hole pairs as well. The rGO nanosheets offer a rapid transferring path for the photogenerated electrons, achieving an efficient charge separation. Therefore, the integration of the three components could achieve collective effect to greatly increase the efficiency of visible-light conversion. The results obtained in this study can be widely applied to design of high efficiency photocatalysts.

Appendix A. Supplementary data

Supplementary data associated with this article can be found, in the online version, at http://dx.doi.org/10.1016/j.apcatb.2016.06.001.

References

[1] A. Kubacka, M. Fernández-García, G. Colón, Chem. Rev. 112 (2012) 1555–1614.
[2] C.C. Chen, W.H. Ma, J.C. Zhao, Chem. Soc. Rev. 39 (2010) 4206–4219.
[3] Y.Q. Qu, X.F. Duan, Chem. Soc. Rev. 42 (2013) 2568–2580.
[4] Y. Ma, X.L. Wang, Y.S. Jia, X.B. Chen, H.X. Han, C. Li, Chem. Rev. 114 (2014) 9987–10043.
[5] M. Fagnoni, D. Dondi, D. Ravelli, A. Albini, Chem. Rev. 107 (2007) 2725–2756.
[6] Y. He, N.B. Sutton, H.H.H. Rijnaarts, A.A.M. Langenhoff, Appl. Catal. B: Environ. 182 (2016) 132–141.
[7] F.J. Heiligtag, W. Cheng, V.R.d. Mendonç, M.J. Süess, K. Hametner, D. Günther, C. Ribeiro, M. Niederberger, Chem. Mater. 26 (2014) 5576–5584.
[8] Y.-J. Cho, H.-i. Kim, S. Lee, W. Choi, J. Catal. 330 (2015) 387–395.
[9] Z.G. Zhao, M. Miyauchi, Angew. Chem. Int. Ed. 47 (2008) 7051–7055.
[10] D. Xu, T. Jiang, D. Wang, L. Chen, L. Zhang, Z. Fu, L. Wang, T. Xie, ACS Appl. Mater. Interfaces 6 (2014) 9321–9327.
[11] L.J. Zhang, S. Li, B.K. Liu, D.J. Wang, T.F. Xie, ACS Catal. 4 (2014) 3724–3729.
[12] A. Tanaka, K. Hashimoto, H. Kominami, J. Am. Chem. Soc. 136 (2014) 586–589.
[13] S.M. Sun, W.Z. Wang, S.Z. Zeng, M. Shang, L. Zhang, J. Hazard. Mater. 178 (2010) 427–433.
[14] Y.Y. Bu, Z.Y. Chen, C.J. Sun, Appl. Catal. B: Environ. 179 (2015) 363–371.
[15] O. Arutanti, A.B.D. Nandiyanto, T. Ogi, T.O. Kim, K. Okuyama, ACS Appl. Mater. Interfaces 7 (2015) 3009–3017.
[16] Y. Ide, M. Matsuoka, M. Ogawa, J. Am. Chem. Soc. 132 (2010) 16762–16764.

[17] D.P. DePuccio, P. Botella, B. O'Rourke, C.C. Landry, ACS Appl. Mater. Interfaces 7 (2015) 1987–1996.

[18] X.L. Yin, J. Liu, W.J. Jiang, X. Zhang, J.S. Hu, L.J. Wan, Chem. Commun. 51 (2015) 13842–13845.

[19] H. Yoo, C. Bae, Y. Yang, S. Lee, M. Kim, H. Kim, Y. Kim, H. Shin, Nano Lett. 14 (2014) 4413–4417.

[20] H.A. Atwater, A. Polman, Nat. Mater. 9 (2010) 205–213.

[21] C. Clavero, Nat. Photonics 8 (2014) 95–103.

[22] A. Tanaka, K. Hashimoto, H. Kominami, J. Am. Chem. Soc. 134 (2012) 14526–14533.

[23] L. Ma, D.S. Wang, J.H. Li, B.Y. Bai, L.X. Fu, Y.D. Li, Appl. Catal. B: Environ. 148 (2014) 36–43.

[24] Q.P. Lu, Z.D. Lu, Y.Z. Lu, L.F. Lv, Y. Ning, H.X. Yu, Y.B. Hou, Y.D. Yin, Nano Lett. 13 (2013) 5698–5702.

[25] Z.H. Zhang, L.B. Zhang, M.N. Hedhili, H. Zhang, P. Wang, Nano Lett. 13 (2013) 14–20.

[26] T. Wang, R. Lv, P. Zhang, C.J. Li, J.L. Gong, Nanoscale 7 (2015) 77–81.

[27] X.Q. An, J.C. Yu, RSC Adv. 1 (2011) 1426–1434.

[28] N. Zhang, M.-Q. Yang, S.Q. Liu, Y.G. Sun, Y.-J. Xu, Chem. Rev. 15 (2015) 10307–10377.

[29] D. Chen, H. Zhang, Y. Liu, J.H. Li, Energy Environ. Sci. 6 (2013) 1362–1387.

[30] M. Khan, M.N. Tahir, S.F. Adil, H.U. Khan, M.R.H. Siddiqui, A.A. Al-warthan, W. Tremel, J. Mater. Chem. A 3 (2015) 18753–18808.

[31] D.C. Marcano, D.V. Kosynkin, J.M. Berlin, A. Sinitskii, Z.Z. Sun, A. Slesarev, L. Alemany, W. Lu, J.M. Tour, ACS Nano 4 (2010) 4806–4814.

[32] J.-W. Liu, Ji. Zheng, J.-L. Wang, J. Xu, H.-H. Li, S.-H. Yu, Nano Lett. 13 (2013) 3589–3593.

[33] G.C. Xi, J.H. Ye, Q. Ma, N. Su, H. Bai, C. Wang, J. Am. Chem. Soc. 134 (2012) 6508–6511.

[34] L. Pan, Q.H. Tao, S.D. Zhang, S.S. Wang, J. Zhang, S.H. Wang, Z.Y. Wang, Z.P. Zhang, Sol. Energy Mater. Sol. Cells 98 (2012) 66–70.

[35] V. Jovic, W.-T. Chen, D.X. Sun-Waterhouse, M.G. Blackford, H. Idriss, G.I.N. Waterhouse, J. Catal. 305 (2013) 307–317.

[36] B.X. Li, T.X. Liu, Y.F. Wang, Z.F. Wang, J. Colloid Interface Sci. 377 (2012) 114–121.

[37] S. Ghosh, M. Saha, S. Paul, S.K. De, Nanoscale 7 (2015) 18284–18298.

[38] H.J. Chen, L. Shao, Q. Li, J.F. Wang, Chem. Soc. Rev. 42 (2013) 2679–2724.

[39] X.B. Cao, Z.F. Lu, L.W. Zhu, L. Yang, L. Gu, L.L. Cai, J. Chen, Nanoscale 6 (2014) 1434–1444.

[40] T.X. Liu, B.X. Li, Y.G. Hao, Z.Y. Yao, Chem. Eng. J. 244 (2014) 382–390.

[41] X.L. Jin, L.Q. Ye, H. Wang, Y.R. Su, H.Q. Xie, Z.G. Zhong, H. Zhang, Appl. Catal. B: Environ. 165 (2015) 668–675.

[42] T. Gunji, A.J. Jeevagan, M. Hashimoto, T. Nozawa, T. Tanabe, S. Kaneko, M. Miyauchi, F. Matsumoto, Appl. Catal. B: Environ. 181 (2016) 475–480.

[43] M. Wu, W.-J. Chen, Y.-H. Shen, F.-Z. Huang, C.-H. Li, S.-K. Li, ACS Appl. Mater. Interfaces 6 (2014) 15052–15060.